Determination of the average orientation of DNA in the octopus sperm *Eledone cirrhossa* through polarized light scattering

D. B. Shapiro, M. F. Maestre, W. M. McClain, P. G. Hull, Y. Shi, M. S. Quinby-Hunt, J. E. Hearst, and A. J. Hunt

The coupled-dipole approximation has been used to model polarized light-scattering data obtained from the sperm of the octopus *Eledone cirrhosa*. Mueller scattering-matrix elements (which describe how a sample alters the intensity and degree of polarization of scattered light) were measured as a function of angle. The sample was modeled as a helical fiber believed to correspond to a DNA protein complex. It was necessary to propose an inherent anisotropy in the polarizability of the fiber in order to fit the data. The direction of the principle axes of the polarizability were determined by comparing the model with experimental data. The results suggest that the 2-nm DNA fibers are perpendicular to the thick fiber that defines the helical geometry of the octopus sperm head.

Key words: Polarized light scattering, Mueller scattering matrix, polarizability, DNA.

1. Introduction

Polarized light scattering has been in use as a biophysical tool for many years.[1,2] In particular, the Mueller scattering-matrix element S_{14} [also known as circular intensity differential scattering, (CIDS)] promised to be useful in the study of helical structures.[3] Yet a lack of good data combined with the complexity of the theory of polarized light scattering from helices has limited its application to specific questions in structural biology. Very few attempts have been made to compare theoretical predictions with measured results of polarized light scattering from helical structures. Mie calculations, which offer an exact solution for spherical particles, show good agreement with experimental data taken of samples of spherical marine algae.[4] Unfortunately, there is no exact solution that describes polarized light scattering from helical structures.

A reasonably successful study that involved both measurements and theoretical predictions of polarized light scattering from helices was carried out by Wells *et al.*[5] This group compared a relatively simple theory based on the first Born approximation to measurements of S_{14} on octopus sperm heads of the species *Eledone cirrhosa*. The large S_{14} of this scatterer was originally discovered by Maestre *et al.*[6] Despite the success of the Wells group in modeling S_{14}, it has been shown that the Born approximation does not predict some of the other Mueller matrix elements for the sperm head as well as it does for S_{14}.[7] For example, the Born approximation predicts S_{34} to be identically zero, but a significant S_{34} is measured.[8] When the polarizability is isotropic, calculations involving the first Born approximation predict a null S_{14}, even for chiral structures. Helical structures are modeled with anisotropic polarizabilities whenever the first Born approximation is used to obtain the nonzero values of S_{14} that are theoretically predicted and experimentally measured for these struc-

When this work was performed the following authors were with the University of California, Berkeley, Berkeley, California 94720: D. B. Shapiro, M. S. Quinby-Hunt, and A. J. Hunt were with the Energy and Environment Division, Lawrence Berkeley Laboratory; M. F. Maestre was with the Cell and Molecular Biology Division, Lawrence Berkeley Laboratory; and J. E. Hearst was with the Chemical Biodynamics Division, Lawrence Berkeley Laboratory. D. B. Shapiro and J. E. Hearst were also with the Graduate Group in Biophysics, University of California, Berkeley; D. B. Shapiro is now with the Department of Chemistry, University of California Santa Cruz, Santa Cruz, California 95064. W. M. McClain and Y. Shi are with the Department of Chemistry, Wayne State University, Detroit, Michigan 48202; P. G. Hull is with the Department of Physics, Tennessee State University, Nashville, Tennessee, 37209-1561. Y. Shi is now with the Department of Chemistry, University of California, Berkeley, Berkeley, California 94720.

Received 12 July 1993; revised manuscript received 29 November 1993.

0003-6935/94/245733-12$06.00/0.

tures.[9] The anisotropy applied in this way, i.e., to describe the asymmetry of the helix, does not necessarily represent an inherent anisotropy in the polarizability of the material being modeled. Finally, the first Born approximation cannot be applied to thick, strongly polarizable structures.[10] Considering the limitations of the first Born approximation, we have used the coupled-dipole approximation to model polarized light-scattering data from the sperm heads. This approximation allows us to determine the direction of an inherent anisotropy in the polarizability in the sperm head and hence to determine the direction of the DNA.

The net electric field at a dielectric material in an applied field was calculated by Kirkwood.[11] An application, known as the coupled-dipole model, of Kirkwood's treatment of dipolar interactions within a dielectric material to the problem of light scattering was originally developed by Purcell and Pennypacker[12] and was further developed by other authors.[13–16] The scatterer is subdivided into discrete subunits. The polarizability is assigned to a point for each subunit through the use of the Maxwell–Garnett theory.[17] Singham *et al.*[18] showed that the coupled-dipole approximation yields identical results for a helix made of spherical subunits (i.e., having an isotropic polarizability) as for a helix composed of prolate spheroidal subunits as long as the thickness of the subunits is the same. Analytical solutions to the coupled-dipole approximation applied to particles in the orientation average have been obtained.[14,19] The analytical approach to the computation of the Mueller matrix in an orientation average is superior to a numerical approach.[20]

In this study we applied a formulation of the coupled-dipole approximation in the orientation average[14] to model measurements made on the helical octopus sperm head. An inherent anisotropy in the polarizability permits an investigation of the nature of DNA packing. The model is limited by the computational power required to model a structure that is composed of many subunits. The sperm head is approximated by a single turn of a helical fiber composed of spherical subunits. The thickness of the fiber in the model is significantly thinner than the corresponding chromatin fiber in the sperm head. Despite the limitations of the model, reasonable agreement with experimental measurements is obtained. The results indicate that the 2-nm DNA double helices are packed with their axes perpendicular to the thick chromatin fiber of the octopus sperm head.

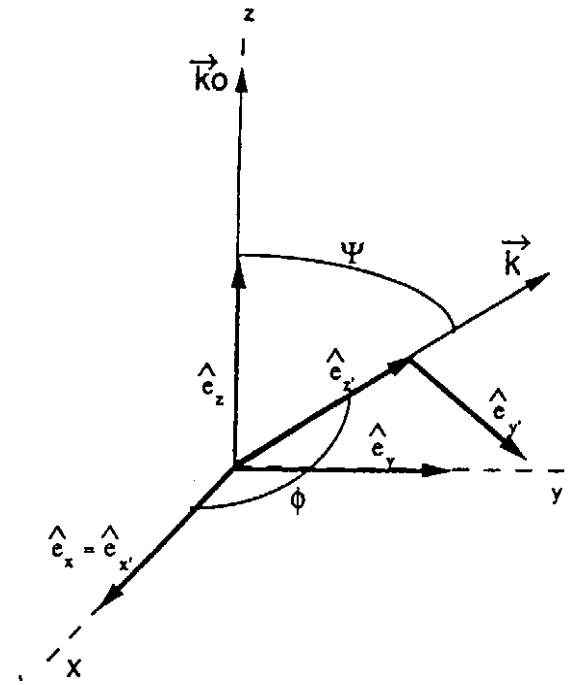

Fig. 1. Coordinate systems of the incidence frame and observation frames. The incidence frame is set along an arbitrary laboratory-fixed frame x, y, z. The incident light described by the propagation vector $\vec{k}_0$ is shown along the z axis. The scattered light described by the propagation vector $\vec{k}$ is defined by the angles Ψ and ϕ. ϕ is the angle between the x axis and $\vec{k}$. Ψ is the angle between the z axis and the projection of $\vec{k}$ onto the z–y plane. When $\phi = \pi/2$ (as shown), the scattering is observed in the y–z plane as a function of the scattering angle Ψ.

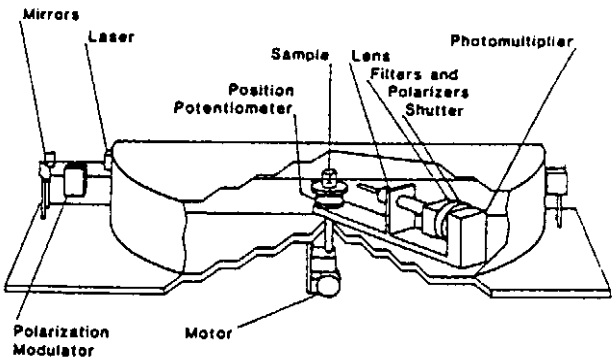

Fig. 2. Scanning polarization-modulation nephelometer. The argon-ion laser produces a beam that is reflected by two mirrors and then traverses a polarizer followed by the photoelastic modulator. The beam is then incident upon the sample on the stand. Scattered light is detected by a photomultiplier tube mounted on a movable arm. Various analyzers housed in the arm allow all of the Mueller matrix elements to be measured.

2. Mueller Matrix Formalism

The Mueller matrix elements are calculated as functions of the scattered electric fields. With the coupled-dipole approximation, the scattered electric field $\vec{E}^s$ is given by

$$\vec{E}^s(\vec{r}_d) = (\vec{\vec{1}} - \hat{k}\hat{k}) \frac{\exp(i\vec{k} \cdot \vec{r}_d)}{r_d} \sum_{j=1}^{N} \exp(i\vec{k}_j \cdot \vec{r}_j) \vec{\vec{\alpha}}_j \cdot \vec{E}_j, \quad (1)$$

where $\vec{r}_d$ is the distance vector from the scatterer to the detector, k is the wave number, $\hat{k}$ is the propagation vector, $\hat{k}\hat{k}$ is the outer product of the propagation unit vectors of the scattered light, $\vec{\vec{\alpha}}_j$, $\hat{k}_j$, $\vec{E}_j$, and $\vec{r}_j$ are the polarizability tensor with units of volume, the propagation vector, the electric field at the jth dipole, and the distance vector of the jth dipole, respectively, and N is the total number of dipoles. Each dipole is excited by the internal field and reradiates. The field

at each dipole is equal to the incident field plus the field resulting from internal dipolar radiation that is due to the other dipoles. The field at the dipole i is given by[15]

$$\vec{E}_i = \vec{E}_i^0 \exp(ikr_i) + \sum_{j\neq i}^{N} a_{ij}\vec{\alpha}_j\vec{E}_j + b_{ij}(\vec{\alpha}_j\vec{E}_j \cdot \hat{n}_{ij})\hat{n}_{ij}, \quad (2)$$

where

$$a_{ij} = \frac{\exp(ikr_{ij})}{r_{ij}}\left(k^2 - \frac{1}{r_{ij}^2} + \frac{ik}{r_{ij}}\right),$$

$$b_{ij} = \frac{\exp(ikr_{ij})}{r_{ij}}\left(-k^2 + \frac{3}{r_{ij}^2} - \frac{3ik}{r_{ij}}\right),$$

$\vec{E}_i^0$ is the incident electric field, $\hat{n}_{ij}$ is a unit vector from the ith to the jth subunit, and r_{ij} is the distance between the ith and jth dipoles. When internal radiation is ignored, only the first term in Eq. (2) need be included. This is equivalent to the first Born approximation applied to a set of point-polarizable groups. The situation is shown in Fig. 1. Let

$$\hat{e}_z = \hat{k}_0, \qquad \hat{e}_z' = \hat{k}, \qquad \hat{e}_x = \hat{e}_x' = \frac{\hat{k}x\hat{k}_0}{|\hat{k}x\hat{k}_0|},$$

$$\hat{e}_y = \hat{e}_z x\hat{e}_x, \qquad \hat{e}_y' = \hat{e}_z' x\hat{e}_x', \quad (3)$$

so that the primed frame is that of the observer and the unprimed frame is the incident frame. Equation (1) can be rewritten as

$$\begin{bmatrix} E_x^s \\ E_y^s \end{bmatrix} = \frac{1}{kr_d}\exp(ikr_d)\begin{bmatrix} J_{11} & J_{12} \\ J_{21} & J_{22} \end{bmatrix}\begin{bmatrix} E_x^0 \\ E_y^0 \end{bmatrix}, \quad (4)$$

where

$$\begin{bmatrix} E_x^0 \\ E_y^0 \end{bmatrix} = \begin{bmatrix} \hat{e}_x \\ \hat{e}_y \end{bmatrix} \cdot \vec{E}^0, \qquad \begin{bmatrix} E_x^s \\ E_y^s \end{bmatrix} = \begin{bmatrix} \hat{e}_x' \\ \hat{e}_y' \end{bmatrix} \cdot \vec{E}^s \quad (5)$$

and

$$\overleftrightarrow{J} = \begin{bmatrix} J_{11} & J_{12} \\ J_{21} & J_{22} \end{bmatrix}$$

is a Jones matrix whose elements are defined by

$$J_{11} = k^3\hat{e}_x \cdot \left[\sum_{a=1}^{N} \vec{\alpha}_a \exp(-i\Delta\vec{k} \cdot \vec{r}_j)\right] \cdot \hat{e}_x,$$

$$J_{12} = k^3\hat{e}_x \cdot \left[\sum_{j=1}^{N} \vec{\alpha}_a \exp(-i\Delta\vec{k} \cdot \vec{r}_j)\right] \cdot \hat{e}_y,$$

$$J_{21} = k^3\hat{e}_y \cdot \left[\sum_{j=1}^{N} \vec{\alpha}_a \exp(-i\Delta\vec{k} \cdot \vec{r}_j)\right] \cdot \hat{e}_x,$$

$$J_{22} = k^3\hat{e}_y \cdot \left[\sum_{j=1}^{N} \vec{\alpha}_a \exp(-i\Delta\vec{k} \cdot \vec{r}_j)\right] \cdot \hat{e}_y. \quad (6)$$

The elements of the Jones matrix describe the manner in which the scatterer alters the polarization state of light, but, because they are complex, they are not direct observables. It is more convenient to describe the scattering in terms of intensities that can be measured directly. A vector may be defined in terms of intensities that completely describe the polarization state of light. This vector is called the Stokes vector. It is defined as

$$\begin{aligned} I &= \langle E_x E_x^* + E_y E_y^* \rangle, && \text{total intensity of light,} \\ Q &= \langle E_y E_y^* - E_x E_x^* \rangle, && \text{linear polarization,} \\ U &= \langle E_y E_x^* + E_x E_y^* \rangle, && \text{diagonal polarization,} \\ V &= \langle i(E_y E_x^* - E_x E_y^*) \rangle, && \text{circular polarization,} \end{aligned} \quad (7)$$

where $\langle \cdots \rangle$ denotes the time average.

The Mueller scattering matrix relates the Stokes vectors of the incident and scattered light. This matrix is a property of the scattering medium and describes how the intensity and polarization state of light will be altered as a function of angle at scattering. It is written as

$$\begin{bmatrix} I_s \\ Q_s \\ U_s \\ V_s \end{bmatrix} = \frac{1}{k^2 r_d^2}\begin{bmatrix} S_{11} & S_{12} & S_{13} & S_{14} \\ S_{21} & S_{22} & S_{23} & S_{24} \\ S_{31} & S_{32} & S_{33} & S_{34} \\ S_{41} & S_{42} & S_{43} & S_{44} \end{bmatrix}\begin{bmatrix} I_i \\ Q_i \\ U_i \\ V_i \end{bmatrix}. \quad (8)$$

The Mueller matrix elements $S_{\eta\nu}$ can be expressed as sums of the products of the Jones matrix elements. The relationships between these quantities is

$$S_{\eta\nu} = \sum_{i,j,m,n=1}^{2} C_{\eta,2(i-1)+j} C^*_{\nu,2(m-1)+n} J_{im} J^*_{jn}, \quad (9)$$

where

$$\overleftrightarrow{C} = \frac{1}{\sqrt{2}}\begin{bmatrix} 1 & 0 & 0 & 1 \\ 1 & 0 & 0 & -1 \\ 0 & 1 & 1 & 0 \\ 0 & i & -i & 0 \end{bmatrix}. \quad (10)$$

The Mueller matrix elements are given in terms of quantities that are related to the Jones matrix elements, i.e., the scattering amplitude matrix elements (see Ref. 17).

3. Experimental Measurements

The scanning polarization-modulation nephelometer used for the present measurements was similar to that developed by one of the authors.[21] A schematic diagram of the apparatus is shown in Fig. 2. An argon-ion laser operated at a wavelength of 457 nm was used as a light source. S_{11} was normalized to the intensity of the scattered light from carbon disulfide at 90°, which is set equal to 1 on a log scale. The other matrix elements S_{ij} were measured with a photoeleastic modulator operating at 50 kHz. A description of this procedure is given in more detail

Fig. 3. Scanning electron micrograph of the sperm head of the octopus *Eledone cirrhosa*.

elsewhere.[17,21] S_{14} and S_{12} are measured by synchronous detection of the 50 kHz and 100 kHz signals, respectively. S_{34} is measured in the same way as S_{14} except for the addition of an analyzer oriented at 45° with respect to the scattering plane. The measured quantity involves S_{14} and S_{34}; deconvolution of the measurement gives S_{34}. At each angle, S_{ij} was divided by the total-intensity matrix element S_{11}. Henceforth, $\mathbf{S}_{ij}$ will refer to the normalized matrix element. Baselines for $\mathbf{S}_{14}$ were measured with 0.49-μm latex spheres. The deviation of $\mathbf{S}_{14}$ from zero for these spheres provides a measure of the uncertainty in $\mathbf{S}_{14}$, which indicates that measurements of $\mathbf{S}_{14}$ are accurate to within 0.3%.

Samples of octopus sperm *Eledone cirrhossa* were obtained in dried form from Prof. J. A. Subirana of the Department of Chemical Engineering, Polytechnique University at Catalonia, Barcelona, Spain. A small portion of the sample was placed in normal saline buffer and adjusted to pH 7.0. An image of the helical sperm head obtained with scanning electron microscopy is shown in Fig. 3. The sample was sonicated for approximately 20 h. Sonication caused the sperm tails to separate from the helical heads and break into small pieces. Figure 4 shows a transmission electron micrograph of the sperm head. This figure suggests that the sperm head is composed of a thick electron-dense helical fiber that is surrounded by a thin membrane. We hypothesize that the sperm-head fiber is a DNA–protein complex that dominates light scattering from the sperm head. The dimensions of the sperm head are pitch = 675–700 nm, radius = 250–300 nm, and length ≈ 43 μm.[5] The radius reported above is an outer radius. The electron micrograph shown in Fig. 4 indicates that the radius of the helical sperm head is approximately 200 nm and that the fiber is approximately 100 nm thick.

Measurements of several matrix elements are shown in Fig. 5. S_{11} is plotted on a log scale. The scattering angle θ is multiplied by sin(θ) to normalize by the scattering volume. The measurement shown for $\mathbf{S}_{14}$ taken at 457 nm, is similar to one previously measured on a different instrument for a different preparation of a sample at 488 nm by Wells *et al.*[5] Both measurements are characterized by a large positive peak at approximately 30°. The measurements by Wells *et al.*[5] of $\mathbf{S}_{14}$ show a stronger peak at 90° than that of the measurement shown in Fig. 5 and show a negative peak at 135° as well. The discrepancies between measurements are probably due to a larger contamination in our sample by Rayleigh scattering from sperm-tail fragments. Wells *et al.*[5] removed sperm-tail fragments from their sample by centrifugation; we were not successful in doing this. Because the sperm heads are strong forward scatterers, small tail fragments in our sample would have a larger relative contribution to the total light scattering away from the forward direction. The S_{14} of the nonhelical sperm tails is zero, but they diminish the measured $\mathbf{S}_{14}$ by contributing to S_{11}. The normalized S_{14} would become $S_{14}/(S_{11_h} + S_{11_t})$, where S_{11_h} and S_{11_t} refer to the S_{11} resulting from the sperm heads and the sperm-tail fragments, respectively. Thus the sperm-tail fragments would tend to reduce the measured, normalized $\mathbf{S}_{14}$, particularly away from the forward direction. Reflections in our scattering cell discussed previously[4] may also explain the difference in our results in the backscattering region. In general our results agree well with those of Wells *et al.*[5]

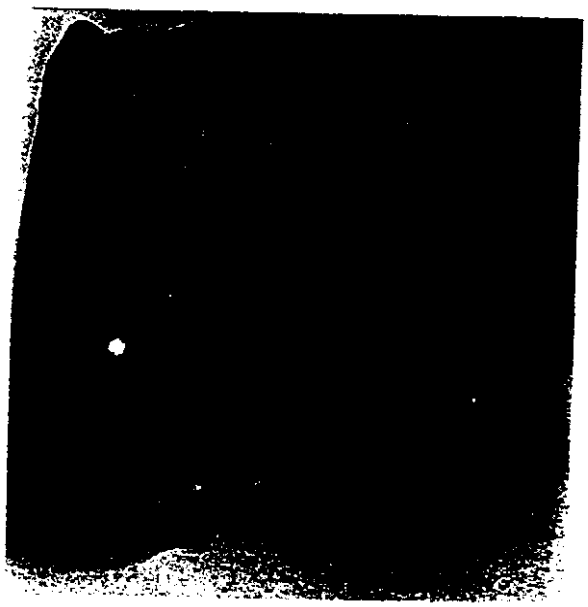

Fig. 4. Transmission electron micrograph of the sperm head of the octopus *Eledone cirrhosa* magnification of 320,000. A dense fiber is seen within the screw-like octopus sperm head.

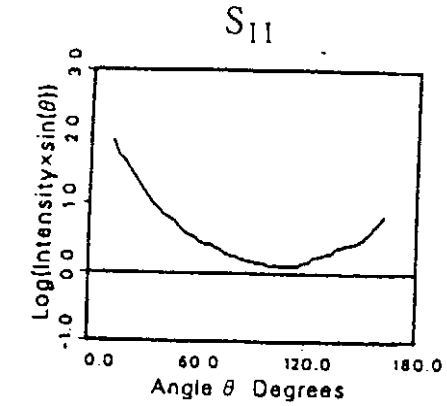

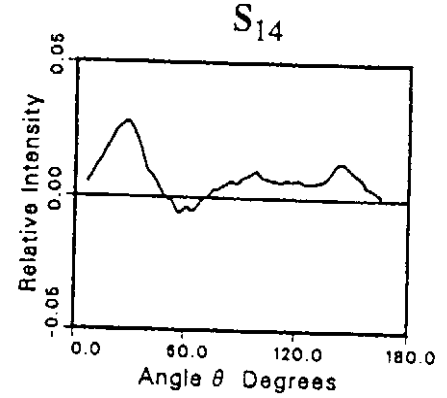

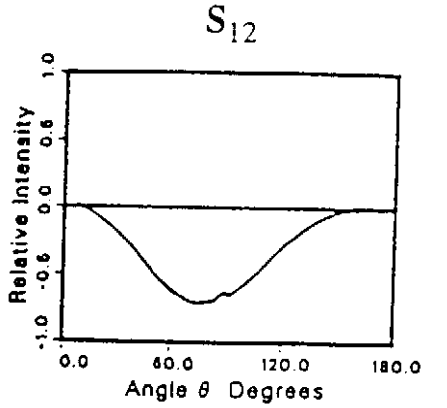

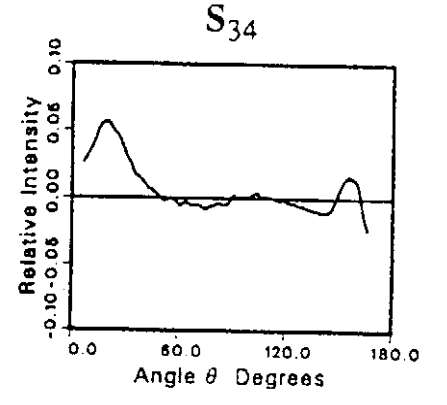

4. Model

We have modeled the angular dependence of several scattering-matrix elements from octopus sperm using the coupled-dipole approximation. Equation (1) represents the scattered electric field with the coupled-dipole approximation. In the coupled-dipole approximation, the electric field at each subunit is equal to the incident field plus the electric field of the radiation from all the other subunits. If a particle is modeled by N dipoles, $3N$ linear equations must be solved simultaneously to determine the net electric field at each dipole location. The solution of the simultaneous equations for finding the electric field at each dipole limits the coupled-dipole method. Because this solution requires the inversion of a large matrix, a high-capacity computer must be employed to carry out the calculations that involve particles composed of many subunits. Although this limitation does not apply to calculations used for the first Born approximation, the coupled-dipole approximation is a more rigorous theory that can be applied to thicker particles and that permits a more realistic study of polarizability.

The present work uses a rigid dipole-array model with full-retarded interdipole coupling.[11,12] Orientation averaging was performed with a modified version of the program PMAT2 that implements the analytical orientation-average method of McClain *et al.*[8,14,19,22] The sperm head was modeled with subunits placed along a helix that is defined by

$$\vec{r}' = a\cos(\theta_h)\hat{x} + a\sin(\theta_h)\hat{y} + \frac{P\theta_h}{2\pi}\hat{z}, \qquad (11)$$

where a is the radius, P is the pitch, and θ_h runs from 0 to $2\pi l$, with l indicating the number of helix turns. The polarizability tensor is defined in terms of a coordinate system local to the helix by

$$\vec{\vec{\alpha}} = \alpha_{tt}\hat{t}\hat{t} + \alpha_{nn}\hat{n}\hat{n} + \alpha_{pp}\hat{p}\hat{p}, \qquad (12)$$

where $\hat{n}$, $\hat{p}$, and $\hat{t}$ are locally defined, mutually orthogonal unit vectors. These unit vectors are usually defined in terms of the tangent, normal, and binormal of the helix.[9,18] In this work, because we want to investigate the direction of the polarizability tensor, these unit vectors are defined so that they can be rotated with respect to the tangent, normal, and binormal directions. The unit vectors $\hat{n}$, $\hat{t}$, and $\hat{p}$ are defined as

$$\begin{aligned}\hat{n} &= \cos(\zeta_1)\sin(\zeta_2)\hat{n}' + \sin(\zeta_1)\sin(\zeta_2)\hat{p}' + \cos(\zeta_2)\hat{t}',\\ \hat{t} &= \cos(\zeta_1)\cos(\zeta_2)\hat{n}' + \sin(\zeta_1)\cos(\zeta_2)\hat{p}' - \sin(\zeta_2)\hat{t}',\\ \hat{p} &= -\sin(\zeta_1)\hat{n}' + \cos(\zeta_2)\hat{p}', \end{aligned} \qquad (13)$$

Fig. 5. Measurements of the Mueller matrix elements from *Eledone cirrhosa*. S_{11} is shown normalized by the intensity of scattering from carbon disulfide at a scattering angle of 90°. The other matrix elements are normalized by S_{11}.

where the angles ζ_1 and ζ_2 define the rotation of the local coordinate system, which is defined by

$$\hat{t}' = -\left(\frac{a}{M}\right)\sin(\theta_h)\hat{x} + \left(\frac{a}{M}\right)\cos(\theta_h)\hat{y} + \left(\frac{P}{2\pi M}\right)\hat{z},$$

$$\hat{p}' = -\left(\frac{P}{2\pi M}\right)\sin(\theta_h)\hat{x} - \left(\frac{P}{2\pi M}\right)\cos(\theta_h)\hat{y} + \left(\frac{a}{M}\right)\hat{z},$$

$$\hat{n} = \cos(\theta_h)\hat{x} + \sin(\theta_h)\hat{y}, \tag{14}$$

with

$$M = \left(a^2 + \frac{P^2}{4\pi^2}\right)^{1/2}.$$

The FORTRAN code was tested by comparison of the results for a randomly oriented ensemble of helices with those computed by Singham *et al.*[19] After correction for an overall minus sign introduced by different definitions of the Stokes parameters, the calculated results for our helices and those reported by Singham *et al.*[19] agreed well.

The components of the polarizability for a given subunit are usually calculated with the Maxwell–Garnett theory.[12,15,17] A general smooth particle is an ellipsoid. The major and minor axes of the ellipsoid correspond to the principal axes of the poalrizability. The strength of the polarizability along each principal axis depends on the shape and nature of the material it represents. If the subunit has an inherent isotropic polarizability, then anisotropy in the polarizability of the subunit will be due to its shape. For an ellipsoidal subunit composed of optically isotropic material,

$$\alpha_i = 4\pi p_{nn}p_{pp}p_{tt}\frac{\varepsilon_r}{3 + 3L_i\varepsilon_r}, \qquad i = tt, nn, pp, \tag{15}$$

where p_{nn}, p_{pp}, and p_{tt} are the lengths of the semiminor and semimajor axes of the ellipsoid, and L_i is a geometrical factor defined by[17]

$$L_i = \frac{p_{nn}pp_{pp}pp_{tt}}{2}\int_0^\infty \frac{dq}{[p_i^2 + q)f(q)]}, \qquad i = tt, nn, pp, \tag{16}$$

where the parameter q disappears at integration and

$$f(q) = \left[\sum_i (q + p_i)^2\right]^{1/2}.$$

ε_r is related to the effective dielectric constant of the subunit ε and to that of the surrounding medium ε_m by the relation

$$\varepsilon_r = \frac{\varepsilon - \varepsilon_m}{\varepsilon_m}. \tag{17}$$

One must calculate the effective dielectric constant of the prolate ellipsoidal subunit. This quantity depends on the bulk dielectric constant of the particle ε_{avg}, that of the surrounding medium ε_m, and the geometry of the subunit.[17]

$$\varepsilon_{avg} = \frac{(1 - f)\varepsilon_m + f\beta\varepsilon}{1 - f + f\beta}, \tag{18}$$

where

$$\beta = \frac{\varepsilon_m}{3}\sum_j \frac{1}{\varepsilon_m + L_j(\varepsilon - \varepsilon_m)}, \qquad j = tt, nn, pp,$$

and f is a volumetric factor equal to $\pi/6$ for ellipsoids. In practice, given ε_m, ε_{avg}, and the dimensions of the subunit, one solves Eq. (18) for the effectiv dielectric constant of the subunit ε. With this value the polarizability components can be calculated for each subunit from Eq. (15). Changing the ratio $\varepsilon_{avg}/\varepsilon_m$ does not affect the calculated polarizabilities. Thus α_i is a function of the size and shape of the subunits and the bulk dielectric constant of the particle relative to the surrounding medium. When the subunit is spherical, all the strengths of the polarizabilities are equal and the polarizability tensor $\vec{\vec{\alpha}}$ is of the form

$$\vec{\vec{\alpha}} = \begin{bmatrix} \alpha_s & 0 & 0 \\ 0 & \alpha_s & 0 \\ 0 & 0 & \alpha_s \end{bmatrix} = \alpha_s\vec{\vec{1}}, \tag{19}$$

where α_s is a scalar quantity characterizing the polarizability of the spherical subunit and $\vec{\vec{1}}$ is the identity matrix. If the subunit is a prolate spheroid with the major axis along the $\hat{t}$ direction, then $p_{nn} = p_{pp}$, and therefore $\alpha_{nn} = \alpha_{pp}$. If the material within the subunit is not optically isotropic, Eq. (15) must be modified. For an optically anisotropic sphere

$$\alpha_j = 4\pi a_s^3\frac{\varepsilon_j - \varepsilon_m}{\varepsilon_j + 2\varepsilon_m}, \qquad j = tt, nn, pp, \tag{20}$$

where ε_j is the strength of the dielectric constant alone a principal axis, and a_s is the radius of the subunit. Thus an anisotropy in the polarizability tensor can arise because of a geometrically anisotropic subunit or a subunit composed of inherently optically anisotropic material.

The model for the octopus sperm head was a single turn of a helical fiber composed of approximately 40 spherical subunits that are approximately 35 nm thick. Because the FORTRAN code used in this work requires an enormous amount of memory, the number of subunits incorporated into our model was severely limited. Earlier work indicated that, for accurate results, the thickness of a subunit should not exceed one tenth the wavelength of light.[18] Thus the thickness of the helix in our model was limited by

the wavelength of light used in the measurements. Only S_{11} is strongly dependent on the number of turns of a helix if there is not a lot of interaction in the helix. This is true as long as there are many subunits in each turn or each subunit on each successive turn is placed in phase with those below it. For example, if a subunit is placed at $\theta_h = \pi/8$, then one must also be placed at $\theta_h = 9\pi/8$. If the subunits on a multiple-turn helix are not placed in this manner, all the normalized Mueller matrix elements are dependent on the number of turns of the helix (although this dependence disappears for a large number of subunits or turns). The independence of $\mathbf{S}_{14}$ to the number of turns is demonstrated in Fig. 6 for a single, thin, weakly interacting helix oriented parallel to the incoming light. $\mathbf{S}_{14}$ is the same for one and two turns of this helix. S_{11} is shown normalized by its magnitude at 0°. Figure 6 shows that S_{11} depends on the number of turns. The changes in S_{11} demonstrate that as the number of turns increases the helix becomes more forward scattering. We have also observed the independence of all the Mueller matrix elements normalized by S_{11} for the helix modeled in Fig. 6 and for helices modeled as a continuous dielectric with the first Born approximation. When the helix is strongly polarizable, some normalized matrix elements do depend on the number of turns. Under these conditions, the induced electric field will affect subunits in neighboring turns. By using only a single turn in our model we have ignored these interactions, although we do account for interactions within a single turn. Because of the availability of computer resources, the number of subunits that were able to incorporate into our model was limited. As a result, our model suffers in its having a limited thickness and only a single turn.

5. Results

The $\mathbf{S}_{14}$ calculated through the use of spherical subunits with isotropic polarizability did not have a magnitude equal to the measured values. The largest calculated $\mathbf{S}_{14}$ found with the assumption of an isotropic polarizability was less than 1.5% with α_s = 5233 nm^3, which is substantially less than is indicated by Fig. 5. In general the calculated $\mathbf{S}_{14}$ should be larger than the measured one because other scatterers in the sample will reduce the measured $\mathbf{S}_{14}$ by contributing to S_{11}. We therefore found it necessary to assume that the modeled helical fiber was composed of material with an inherently anisotropic polarizability. This inherent anisotropy could correspond to ordered packing of the DNA in the sperm head.

S_{34} was most sensitive to the absolute strength of the polarizability. The absolute magnitude of the polarizability was originally set at a value computed by the theory outlined in Section 4 [Eqs. (15)–(20)] with the dielectric constant of the material set at 2.0 and that of the medium at 1.8. The magnitude of the polarizability was then refined by comparisons of the magnitude of calculated $\mathbf{S}_{34}$ with the measured magnitudes. Calculations attempted with a polarizability that was too large, resulted in poor agreement of $\mathbf{S}_{12}$ and $\mathbf{S}_{14}$ with measured values. When the polarizability is too large, the coupled-dipole approximation breaks down because the interaction between subunits becomes too large.

Mueller matrix elements were calculated for a wavelength in the medium (index of refraction = 1.3) of 352 nm. The following parameters in the model were varied in an attempt to replicate the measured Mueller matrix elements ($\mathbf{S}_{12}$, $\mathbf{S}_{14}$, and $\mathbf{S}_{34}$): pitch, radius, degree of anisotropy of the polarizability, and

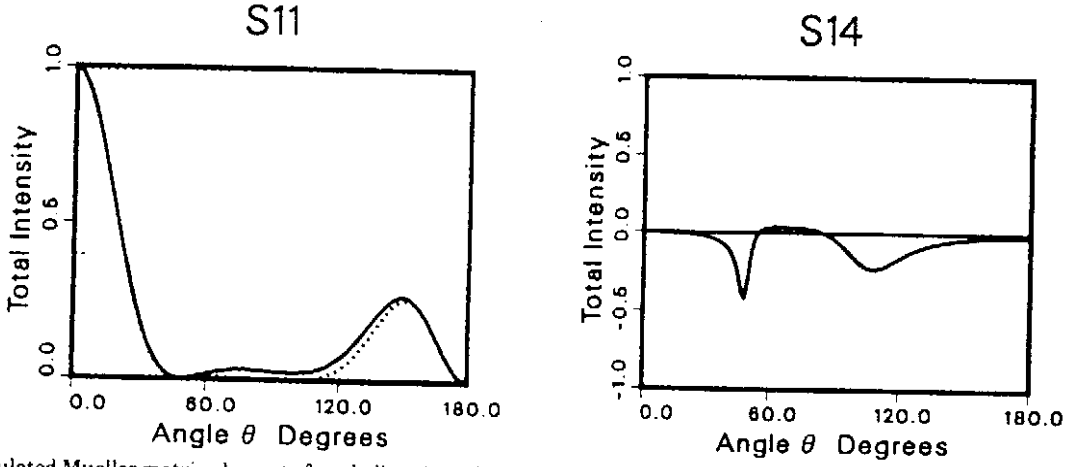

Fig. 6. Calculated Mueller matrix elements for a helix oriented parallel to the incoming light. The helix has a pitch and radius of 250 nm for a wavelength of 500 nm. The calculation for a single turn of the helix is shown by the solid curve, and the dotted curve represents the calculation of two turns of the helix. (a) S_{11} normalized by its value of the scattering angle 0°. The scattering of the two-turn helix is much more forward scattering than the single-turn helix, as evidenced by its value at 90°. (b) $\mathbf{S}_{14}$ normalized by S_{11}, shown to be independent of the number of helix turns.

the direction of the principle axes of the polarizability with respect to the helix. The best fit [Fig. 7(a)] was obtained with a pitch = 650 nm, radius = 190 nm, and polarizability strengths $\alpha_{tt} = 6433\ \text{nm}^3$, and $\alpha_{pp} = \alpha_{nn} = 2617\ \text{nm}^3$. The direction of the principle axis of polarizability for α_{tt} was 9° from the tangent to the helical fiber. The anisotropy ratio $(\alpha_{tt} - nn)/(\alpha_{tt} + \alpha_{nn})$ was 42%.

The largest strength of the polarizability is close to tangent to the helix. Figures 7(b) and 7(c) show the calculated matrix elements when that strength is placed along the normal or binormal. Comparisons with the experimental results shown in Fig. 5 indicate that the large component of the polarizability is close to the tangent of the helical fiber. The calculated S_{14} in Figure 7(a) also agrees well with previous data reported by Wells *et al.*[5]

Lack of agreement between the measured and calculated results may be partially due to the presence of sperm-tail fragments in the sample. These fragments are thin and small compared with the sperm heads and the wavelength of light. Their contribution to the measured Mueller matrix elements may then be assumed to be that of a Rayleigh

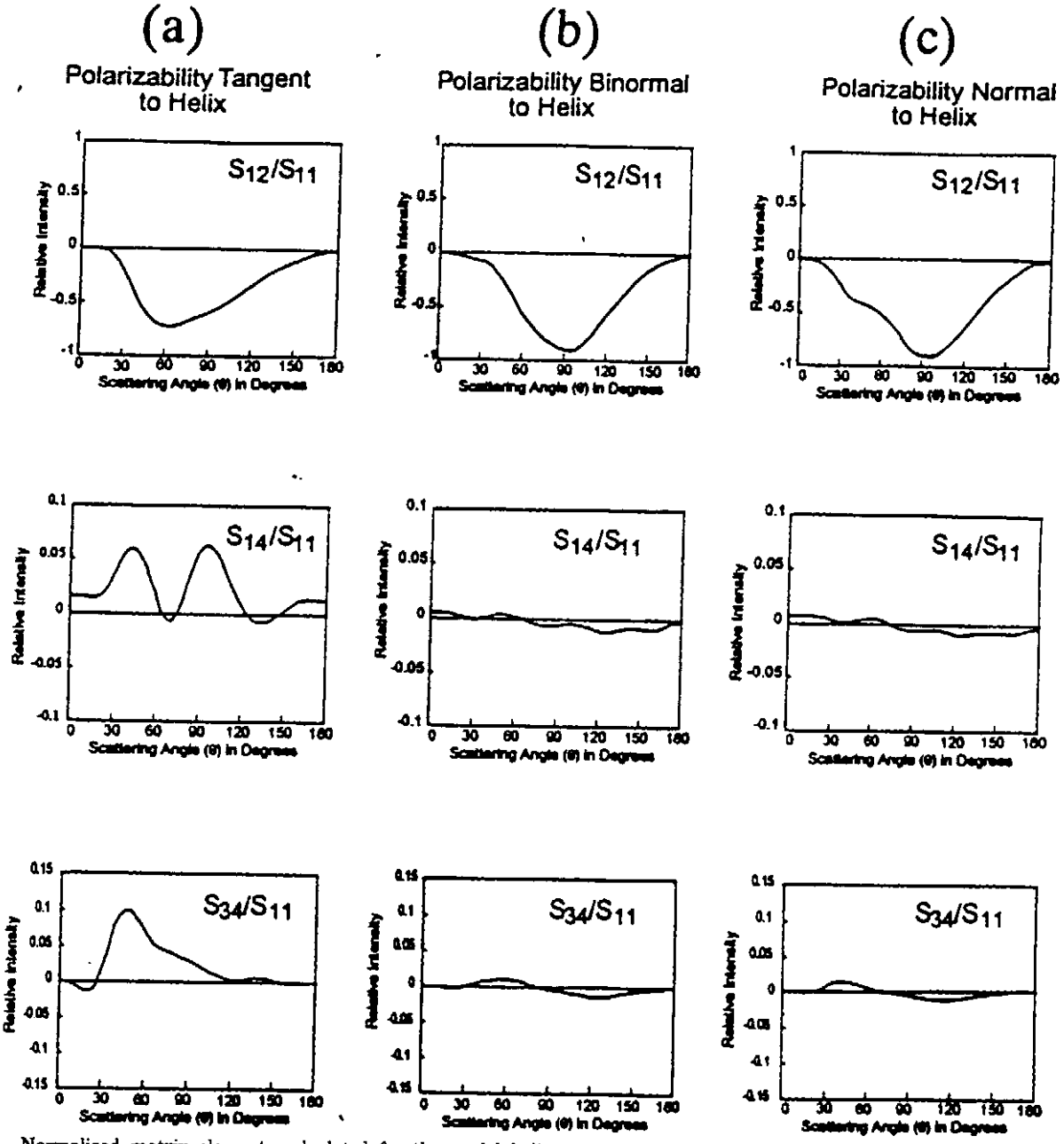

Fig. 7. Normalized matrix elements calculated for the model helix in the orientation average: (a) The largest strength of the polarizability is close to tangent to the helix: $\zeta_1 = \pi/4$, $\zeta_2 = 31\pi/20$. $\alpha_{tt} = 6433\ \text{nm}^3$, $\alpha_{pp} = 2617\ \text{nm}^3$, and $\alpha_{nn} = 2617\ \text{nm}^3$. (b) The largest strength of the polarizability is along the binormal to the helix: $\zeta_1 = 0$, $\zeta_2 = 3\pi/2$, $\alpha_{pp} = 6433\ \text{nm}^3$, $\alpha_{tt} = 2617\ \text{nm}^3$, and $\alpha_{nn} = 2617\ \text{nm}^3$. (c) The largest strength of the polarizability is along the normal to the helix $\hat{n}'$: $\zeta_1 = 0$, $\zeta_2 = 3\pi/2$, $\alpha_{nn} = 6433\ \text{nm}^3$, $\alpha_{tt} = 2617\ \text{nm}^3$, and $\alpha_{pp} = 2617\ \text{nm}^3$.

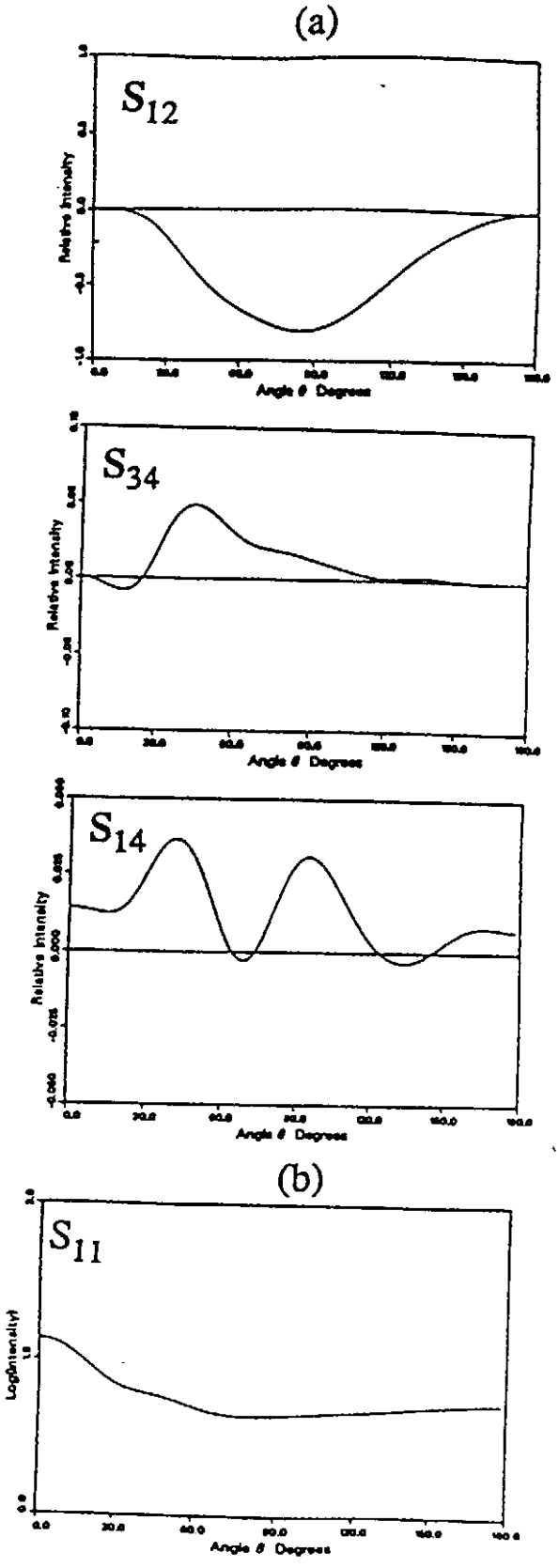

Fig. 8. Rayleigh correction: (a) Mueller matrix elements calculated for Fig. 7(a) corrected for the presence of Rayleigh scatterers according to Eq. (21) and relation (22), with $\gamma = 10$. (b) S_{11} for the model helix with the same parameters used for the results shown in Fig. 7(a). This is the S_{11_c} used for the Rayleigh correction.

scatterer. To investigate the effect of the sperm tails, the calculations were repeated with a correction for the presence of Rayleigh scatterers. Rayleigh scatterers are characterized by the following Mueller matrix elements:

$$S_{14} = S_{34} = 0, \quad S_{11} = \gamma[1 + \cos^2(\theta)],$$
$$S_{12} = \gamma[\cos^2(\theta) - 1], \tag{21}$$

where γ corresponds to the magnitude of the contribution from the Rayleigh scatterers. The corrected values of the Mueller matrix elements are calculated by addition of the calculated matrix element for the helical sperm-head fiber to that of the Rayleigh scatterer by

$$S_{ij} \rightarrow S_{ij_c} + S_{ij_r} \tag{22}$$

where S_{ij_c} and S_{ij_r} are the matrix elements from the original calculation for the helical fiber and the Rayleigh scatterers. Thus, for $\mathbf{S_{12}}$

$$\frac{S_{12}}{S_{11_h}} \rightarrow \frac{S_{12_c} + S_{12_r}}{S_{11_c} + S_{11_r}}. \tag{23}$$

The amount of scattering attributable to Rayleigh scatterers was determined by comparison with the experiment. The results of this correction, which was applied to all the calculated matrix elements, for an amount of Rayleigh scatterers such that they scatter as much as the helical sperm fibers at 90° is shown in Fig. 8(a). Figure 8(b) shows S_{11_c} calculated for one turn of the helix.

6. Discussion and Conclusions

We have modeled the polarized light scattering from octopus sperm using the coupled-dipole approximation. Simultaneous modeling of several Mueller matrix elements helps to limit the combination of parameters that describe the helix. A change in one parameter causes the calculated $\mathbf{S_{14}}$ to become more like the measured value, but $\mathbf{S_{34}}$ may become less like the measurement. This same argument applies to the Rayleigh correction used for Fig. 8. When the relative contribution to the scattered light from the Rayleigh scatterers is too large, the calculated $\mathbf{S_{12}}$ becomes less like the measured data.

Comparison of S_{11} in Fig. 8(b) with the measurements shown in Fig. 5 reveals that the measured S_{11} indicates much more forward scattering than is indicated by the calculated value. The thickness of the helical fiber used in the model was significantly smaller than the apparent thickness of the real DNA–protein fiber and may have been responsible for the diminished forward scattering in the calculations. This can also be attributed to the calculation being made for only one turn of the helix. As mentioned above, the Mueller matrix elements, when normalized by the total intensity element S_{11}, do not depend heavily on the number of helix turns, but S_{11} becomes more forward scattering when it is calculated for a

helix having more turns. This dependence of S_{11} on the number of helix turns should hold true as long as the length of the particle does not become too many times greater than the wavelength; for long helices the shape of S_{11} should not change. The data show that the sperm heads are very forward scattering (see Fig. 1). The S_{11} would have appeared even more forward scattering without the Rayleigh scatterers present. Therefore the Rayleigh scatterers in the sample may have diminished the normalized S_{14} and S_{34} even more than is shown in Fig. 8.

Because they are small and thin, we have assumed that the sperm-tail fragments scatter as if they were Rayleigh particles. If this assumption is incorrect, then their contributions to the measured matrix elements described in relation (22) are not accurate. For example, if the fragments are stronger scatterers, their contribution to S_{34} would become nonzero. Even so, their apparent size would indicate that compared with the sperm heads their S_{34} would be quite small.

We have chosen to model $\mathbf{S}_{12}$, $\mathbf{S}_{14}$, and $\mathbf{S}_{34}$ because these elements are not difficult to measure and are representative of three classes of elements: the dipole elements S_{12}, the helicity elements S_{14}, and the retardation elements S_{34}.[13,21] S_{12} is sensitive to general size parameters of a particle and is always observed for any type of particle. S_{14} is sensitive to the chiral nature of a particle; it is zero for an ensemble of randomly oriented particles unless the particles are chiral. S_{34} is sensitive to size and refractive index; it is zero for small or thin particles.

Calculations that used the polarizability theory outlined in Eqs. (15)–(18), when applied to spherical subunits that make up the helix, did not result in values of $\mathbf{S}_{14}$ that were as large as the measured values. It was necessary to incorporate spherical subunits with anisotropic dipoles into our model to best fit the data. The magnitude of $\mathbf{S}_{14}$ is very sensitive to the degree of anisotropy in the polarizability. The magnitude of $\mathbf{S}_{34}$ is largely dependent on the magnitude of the polarizability. The number of nodes in $\mathbf{S}_{14}$ was sensitive to the radius used in the model. This observation is consistent with that of an earlier study made with the first Born approximation.[9] The direction of the polarizability affected the shape of all the Mueller matrix elements. The best results were obtained when the strongest polarizability was nearly tangent to the helix. Although the direction 9° from the tangent is based on somewhat subjective comparisons of calculations with measurements, Fig. 7 shows that the greatest polarizability lies closer to the tangent than to the normal or binormal directions. Because the polarizability of DNA is strongest in the plane of the base pairs[23] (i.e., perpendicular to the 2-nm double helix), this result indicates that the DNA double helices in the sperm head lie perpendicular to the helical, thick sperm-head fiber.

The most in-depth study of the ultrastructure of the sperm of *Eledone cirrhosa* was conducted by Maxwell.[24] That author concluded that the rigid helical structure of the sperm head is due to its chromatin. That the shape of the sperm head is due to the chromatin has also been suggested by other researchers for mammals, birds, insects, and annelids.[25] Maxwell found that DNA begins to form 10-nm fibers during spermiogenesis.[24] Maxwell also reported that the 10-nm fibers condensed further as spermiogensis progressed, but he did not propose an arrangement of the DNA within its final condensed form.[24]

The DNA's being perpendicular to the sperm-head fiber is consistent with several models of higher-order DNA organization in sperm (Figs. 9).[26–31] The 10-nm fiber referred to by Maxwell may be similar to the intermediate fiber proposed for the DNA–protamine complex formed in mammalian sperm.[26] In mammalian sperm it is believed that a primary condensation of DNA occurs when 2-nm strands of DNA lie parallel to one another with one in the major groove of the other [intermediate fiber, Fig. 9(b)].[26,27] The final level of organization of DNA in mammalian sperm may be similar to that in somatic cells.[27,28] The DNA intermediate fiber forms loops that are attached to a nuclear matrix, and the fibers end up perpendicular to the axis of the larger fiber that is formed by the

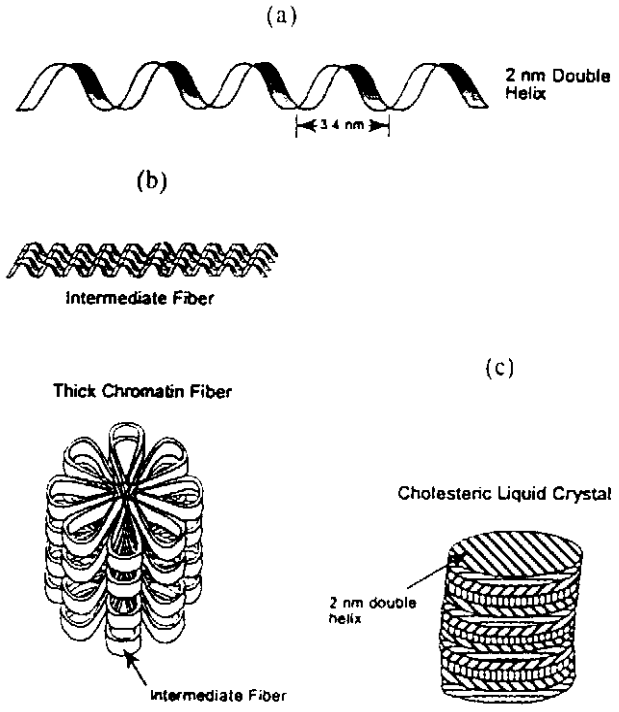

Fig. 9. Two models for higher organization of DNA in mammalian sperm. (a) Double-helix structure of noncondensed mammalian DNA. (b) DNA molecules lie parallel to each other to form an intermediate fiber.[25] The intermediate fibers are attached to a protein matrix in loops in a manner similar to that in somatic cells.[26,27] (c) The Cholesteric model proposed for stallion sperm.[28,29] The DNA molecules are parallel to each other on each horizontal plane. Their average direction rotates from one plane to the next.

looped fibers and the nuclear matrix. The final fiber is approximately 840 nm thick in somatic cells, whereas the loops are nearly 60% smaller in sperm cells.[28] In sperm cells the 2-nm DNA strands would be perpendicular to the chromatin fiber. An alternative model [Fig. 9(c)] for stallion sperm DNA proposes that the DNA forms a structure similar to that of a cholesteric crystal.[29,30] In the equine model the 2-nm DNA strands are proposed to be parallel to each other within a cross section of a thick fiber. The average direction of the DNA rotates from one cross section to the next and results in a characteristic pitch to the thick fiber. The DNA is perpendicular to the axis of the thick fiber in this cholesteric-crystal model. Finally evidence has recently been reported that indicates that the DNA within mammalian sperm cells is organized into numerous toroidal structures with a 90-nm outside diameter.[31] If such structures are similarly present in *Eledone cirrhossa* and are organized in a linear fashion, then the resulting fiber would be 90 nm in diameter with the 2-nm DNA strands perpendicular to the primary axis. Thus the DNA is believed to be perpendicular to the thick fiber in several models of higher-organization DNA in sperm cells.

In summary, we have determined that the average direction of the 2-nm DNA strands are perpendicular to the thick, chromatin fiber in the octopus sperm head by comparing polarized light-scattering measurements to theoretical calculations. Thus, the technique of polarized light scattering has been used to obtain information in structural biology that has not been otherwise obtained with microscopy techniques. With the extension of measurements to smaller wavelengths with which smaller structures can be studied, polarized light could become a more valuable biophysical tool.

We are indebted to T. Hayes for his work in transmission electron microscopy. We thank S. Goolsby for help in preparing the octopus sperm samples. This work was supported by the Office of Naval Research under grants DE-AC03-76SF00098 and N00014-92-J-1284, which were awarded to A. J. Hunt and P. G. Hull, and by the National Institutes of Health under grant AI22636 awarded to W. M. McClain and grant AI08427 awarded to M. F. Maestre.

References

1. P. J. Wyatt, "Identification of bacterial by differential light scattering," Nature (London) **21**, 1257–1259 (1969).
2. W. S. Bickel, J. F. Davidson, D. R. Huffman, and R. Kilkson, "Application of polarization effects in light scattering: a new biophysical tool," Proc. Natl. Acad. Sci. (USA) **73**, 486–490 (1976).
3. B. P. Dorman and M. F. Maestre, "Experimental differential light scattering corrections to the circular dichroism of T2 bacteriophage," Proc. Natl. Acad. Sci. (USA) **70**, 255–259 (1973).
4. M. S. Quinby-Hunt, A. J. Hunt, K. Lofftus, and D. Shapiro, "Polarized-light scattering studies of marine *Chlorella*," Limnol. Oceanogr. **34**, 1587–1600 (1989).
5. K. S. Wells, D. A. Beach, D. Keller, and C. Bustamante, "An analysis of circular intensity differential scattering measurements: studies on the sperm cell of *Eledone cirrhosa*," Biopolymers **25**, 2043–2064 (1986).
6. M. F. Maestre, C. Bustamante, T. L. Hayes, J. A. Subirana, and I. Tinoco, Jr., "Differential scattering of circularly polarized light by the helical sperm head from the octopus *Eledone cirrhosa*," Nature (London) **298**, 773–774 (1982).
7. D. B. Shapiro, A. J. Hunt, M. S. Quinby-Hunt, M. F. Maestre, P. G. Hull, and K. Kah-Eng, "A theoretical and experimental study of polarized light scattering by helices," in *Ocean Optics XI*, G. D. Gilbert, ed., Proc. Soc. Photo-Opt. Instrum. Eng. **1750**, 56–73 (1992).
8. W. M. McClain, J. A. Schauerte, and R. A. Harris, "Model calculations of intramolecular effects in Rayleigh scattering from solutions of macromolecules," J. Chem. Phys. **80**, 606–616 (1984).
9. C. Bustamante, M. F. Maestre, and I. Tinoco, Jr., "Circular intensity differential scattering of light by helical structures. II. Applications," J. Chem. Phys. **73**, 6046–6055 (1980).
10. C. Bustamante, M. F. Maestre, D. Keller, and I. Tinoco, Jr., "Differential scattering (CIDS) of circularly polarized light by dense particles," J. Chem. Phys. **80**, 4817–4823 (1984).
11. J. G. Kirkwood, "On the theory of dielectric polarization," J. Chem. Phys. **4**, 592–601 (1936).
12. E. M. Purcell and C. R. Pennypacker, "Scattering and absorption of light by nonspherical dielectric grains," Astrophys. J. **186**, 705–714 (1973).
13. S. Zeitz, A. Belmont, and C. Nicollini, "Differential scattering of circularly polarized light as a unique probe of polynucleosome superstructures," Cell Biophys. **5**, 163–187 (1983).
14. W. M. McClain and W. A. Ghoul, "Elastic light scattering by randomly oriented macromolecules: computation of the complete set of variables," J. Chem. Phys. **84**, 6609–6622 (1986).
15. S. B. Singham and G. C. Salzman, "Evaluation of the scattering matrix of an arbitrary particle using coupled-dipole approximation," J. Chem. Phys. **84**, 2658–2667 (1986).
16. P. G. Hull, A. J. Hunt, M. S. Quinby-Hunt, and D. B. Shapiro, "Coupled-dipole approximation: predicting scattering by nonspherical marine organisms," in *Underwater-Imaging, Photography, and Visibility*, R. W. Spinrad, ed., Proc. Soc. Photo-Opt. Instrum. Eng. **1537**, 21–29 (1991).
17. C. F. Bohren and D. R. Huffman, *Absorption and Scattering of Light by Small Particles* (Wiley, New York, 1983).
18. S. B. Singham, C. W. Patterson, and G. C. Salzman, "Polarizabilities for light scattering from chiral particles," J. Chem. Phys. **85**, 763–770 (1986).
19. M. K. Singham, S. B. Singham, and G. C. Salzman, "The scattering matrix for randomly oriented particles," J. Chem. Phys. **85**, 3807–3815 (1986).
20. W. M. McClain, D. Tian, and W. A. Ghoul, "Comparison of numerical and analytical orientation average methods in polymer light scattering," J. Chem. Phys. **87**, 4986–4994 (1987).
21. A. J. Hunt and D. R. Huffman, "A new polarization-modulated light scattering instrument," Rev. Sci. Instrum. **44**, 1753–1762 (1973).
22. D. Tian and W. M. McClain, "Nondipole light scattering by partially oriented ensembles. I. Numerical calculations and symmetries," J. Chem. Phys. **90**, 4783–4794 (1989).
23. N. T. Stellwagen, "Electrooptics of polynucleitides and nucleic acids," in *Molecular Electroptics*, C. O'Kanski, ed. (Dekker, New York, 1978), pp. 645–683.

24. W. L. Maxwell, "Spermiogenesis of *Eledone cirrhosa* Lamark (cephalopoda, octopoda)," Proc. R. Soc. London Ser. B **186,** 181–190 (1974).
25. D. W. Fawcett, W. A. Anderson, and D. M. Phillips, "Morphogenic factors influencing the shape of the sperm head," Dev. Biol. **26,** 220–251 (1971).
26. R. Balhorn, "A model for the structure of chromatin in mammalian sperm," J. Cell Biol. **93,** 298–305 (1982).
27. R. H. Getzenberg, K. J. Pienta, W. S. Ward, D. S. Coffey, "Nuclear structure and the three-dimensional organization of DNA," J. Cell. Biol. **47,** 289–299 (1991).
28. W. S. Ward, A. W. Partin, and D. S. Coffey, "DNA loops in mammalian spermotozoa," Chromosoma **98,** 153–159 (1989).
29. F. Livolant, "Cholesteric organization of DNA in the stallion sperm head," Tiss. Cell **16,** 535–555 (1983).
30. M. L. Sipski and T. E. Wagner, "The total structure and organization of chromosomal fibers in Eutherian sperm nucleii," Biol. Reprod. **16,** 428–440 (1977).
31. N. V. Hud, M. J. Allen, K. H. Downing, J. Lee, and R. Balhorn, "Identification of the elemental packing unit of DNA in mammalian sperm cells by atomic force microscopy," Biochem. Biophys. Res. Commun. **193,** 1347–1354 (1993).